



HAL
open science

Symmetry breaking organizes the brain's resting state manifold

Jan Fousek, Giovanni Rabuffo, Kashyap Gudibanda, Hiba Sheheitli, Viktor Jirsa, Spase Petkoski

► **To cite this version:**

Jan Fousek, Giovanni Rabuffo, Kashyap Gudibanda, Hiba Sheheitli, Viktor Jirsa, et al.. Symmetry breaking organizes the brain's resting state manifold. Cold Spring Harbor Laboratory Press, 2023, 10.1101/2022.01.03.474841 . hal-04086340

HAL Id: hal-04086340

<https://amu.hal.science/hal-04086340>

Submitted on 2 May 2023

HAL is a multi-disciplinary open access archive for the deposit and dissemination of scientific research documents, whether they are published or not. The documents may come from teaching and research institutions in France or abroad, or from public or private research centers.

L'archive ouverte pluridisciplinaire **HAL**, est destinée au dépôt et à la diffusion de documents scientifiques de niveau recherche, publiés ou non, émanant des établissements d'enseignement et de recherche français ou étrangers, des laboratoires publics ou privés.



Distributed under a Creative Commons Attribution - NonCommercial - NoDerivatives 4.0 International License

1 Symmetry breaking organizes the brain's resting 2 state manifold

3 Jan Fousek¹, Giovanni Rabuffo¹, Kashyap Gudibanda¹, Hiba
4 Sheheitli¹, Viktor Jirsa¹, and Spase Petkoski¹

5 ¹Aix Marseille University, INSERM, INS, Institut de Neurosciences
6 des Systèmes, 13005 Marseille, France

7 March 12, 2023

8 **Abstract**

9 Spontaneously fluctuating brain activity patterns that emerge at rest
10 have been linked to brain's health and cognition. Despite detailed descrip-
11 tions of the spatio-temporal brain patterns, our understanding of their
12 generative mechanism is still incomplete. Using a combination of compu-
13 tational modeling and dynamical systems analysis we provide a mechanis-
14 tic description of the formation of a resting state manifold via the network
15 connectivity. We demonstrate that the symmetry breaking by the connec-
16 tivity creates a characteristic flow on the manifold, which produces the
17 major data features across scales and imaging modalities. These include
18 spontaneous high amplitude co-activations, neuronal cascades, spectral
19 cortical gradients, multistability and characteristic functional connectiv-
20 ity dynamics. When aggregated across cortical hierarchies, these match
21 the profiles from empirical data. The understanding of the brain's resting
22 state manifold is fundamental for the construction of task-specific flows
23 and manifolds used in theories of brain function such as predictive cod-
24 ing. In addition, it shifts the focus from the single recordings towards
25 brain's capacity to generate certain dynamics characteristic of health and
26 pathology.

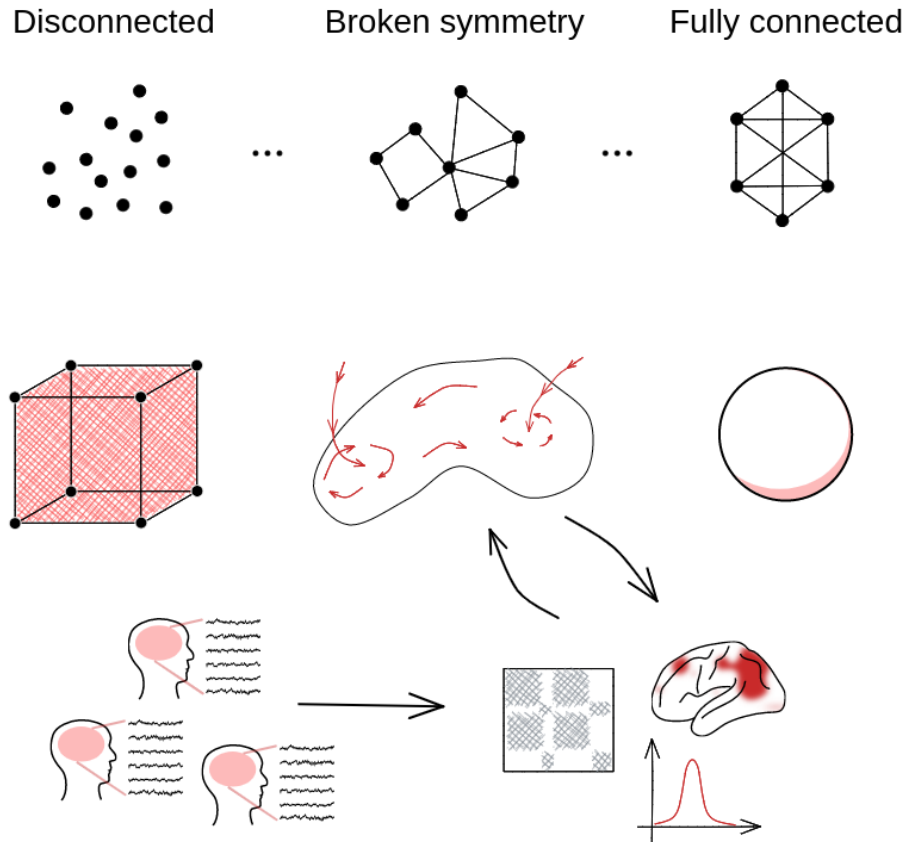
27 **1 Introduction**

28 The human brain at rest exhibits remarkable richness of neural activity struc-
29 tured both in time and space. Early computational modeling studies explored
30 how these spontaneous fluctuations are constrained and how their organisation
31 is shaped by the anatomic connectivity [1–4] enabling to start disentangling
32 the mechanisms of the resting state dynamics *in silico*. A substantial body of
33 work has related the emergent activity patterns at rest to the brain functional
34 networks involved in task conditions [5, 6], and shown that the spatio-temporal

35 variability of resting-state activity possesses functional significance [7–9], rel-
36 evance to cognitive task performance [10], consciousness levels [11], changes
37 during ageing [12, 13], mental disorders [14], and neurodegenerative diseases
38 (e.g. Alzheimer’s dementia; [15]). The structure of the resting state dynam-
39 ics changes over time [16] and is characterized by a range of properties such
40 as metastability [17, 18], event-like coactivations [19–21] and traveling waves
41 [22]. However, our understanding of the mechanisms underlying these spatio-
42 temporal patterns of the brain activity at rest is still incomplete [23] and whole
43 brain network models have a crucial role to play on that front [24].

44 There is general agreement that the resting brain operates near critical-
45 ity [25]. This is supported by a large range of analyses performed on simu-
46 lated and empirical data using network based measures (functional connectivity,
47 functional connectivity dynamics), information theoretical measures (entropy,
48 ignition) and descriptions of spatiotemporal dynamics (avalanches, cascades).
49 Modeling efforts provide further evidence for the close relationship between the
50 empirical data features and the properties of the structural network, local dy-
51 namics, coupling strength, neural gain [4, 13, 26–31]. The resting state dynamics
52 can then be understood as noise-driven fluctuations of brain activity, operat-
53 ing near criticality and constrained by the brain connectivity [2, 32]. However,
54 none of the above qualifies as a description of a mechanism. Descriptions of
55 mechanisms require formulation in terms of causal activities of their constituent
56 entities and render the end stage, in our context the resting state dynamics,
57 intelligible by showing how it is produced [33]. To explain is thus not merely to
58 redescribe one regularity (e.g. functional connectivity dynamics, or maximiza-
59 tion of entropy) as a series of several (such as near-criticality, cascades, ignition).
60 Rather, explanation involves revealing the productive relation between causal
61 activities linked to their constituent entities.

62 In this paper we aim to remedy this situation and provide this explanation
63 using Structured Flows on Manifolds (SFMs) [34–38]. SFMs is a mathematical
64 framework explaining how low dimensional dynamics, reflecting generative sets
65 of rules underlying behavior, emerges in high-dimensional nonlinear systems,
66 specifically dynamical systems on networks modeling macroscale brain dynam-
67 ics. When properly linked to the network’s constituent entities (functional nodes
68 and connectivity), we will demonstrate how their causal activities lead to the
69 formation of brain’s resting SFM, comprising all its dynamic signatures (see
70 Figure 1). If we distill the previous reports of brain resting state data analysis
71 from the dynamical systems point of view, we arrive at the following main em-
72 pirical signatures that should be part of the end stage of a successful mechanistic
73 description: bistability of single region activation [39–41], low-dimensionality of
74 the global system dynamics in state space [7, 42, 43], cascade propagation [44],
75 multistability of recurrent coactivation spatial patterns [18, 45] and their non-
76 trivial temporal dynamics or intermittency [21, 32, 46]. These signatures will
77 constitute the key features of what we will describe as structured flows on the
78 low dimensional resting state manifold.



79

80 **Figure 1: Structured flows on manifolds as focus of resting state**
 81 **characterization.** With respect to the structure of the connectivity of the
 82 dynamical system, we consider spectrum defined by the two symmetrical limit
 83 cases: fully connected and fully disconnected network. Driven by noise, the
 84 disconnected system exhibits fully statistical, high-dimensional dynamics - it
 85 explores the whole state space in an equidirectional manner. On the other hand,
 86 the dynamics of the fully connected system is fully constrained corresponding to
 87 a $SO(n)$ hypersphere with zero flow. The dynamics on the sparsely connected
 88 system leads to an object in between - a low-dimensional attractive manifold
 89 with an associated flow (SFM). It is this object we wish to put in the center of
 90 interest and characterize. While the SFM object remains the same, connections
 91 are made to data of various modalities with the help of suitable data features.

92 2 Results

93 In what follows we employ whole-brain modeling to study the low dimensional
 94 manifold and the associated structured flows of the spontaneous resting state

95 dynamics, and how these relate to the structural connectome. We constructed a
96 brain network model (BNM) in the Virtual Brain [47] using the two-dimensional
97 mean-field model of an ensemble of quadratic integrate-and-fire neurons ([48];
98 MPR) to govern the regional dynamics coupled with a connectome derived from
99 a subject from the Human Connectome Project [49]. We applied Balloon-
100 Windkessel model [50] to the simulated neuronal mass activity to generate
101 realistic BOLD signals. From these, we computed the Dynamical Functional
102 Connectivity (dFC) that captures the changes in the system’s dynamics on the
103 slow time scale, which we compared with empirical recordings. The fast neu-
104 ronal activity is decomposed in a $2N$ -dimensional state space using Principal
105 Component Analysis (PCA) to unveil the low-dimensional manifold on which
106 the system evolves (see Materials and Methods for more details).

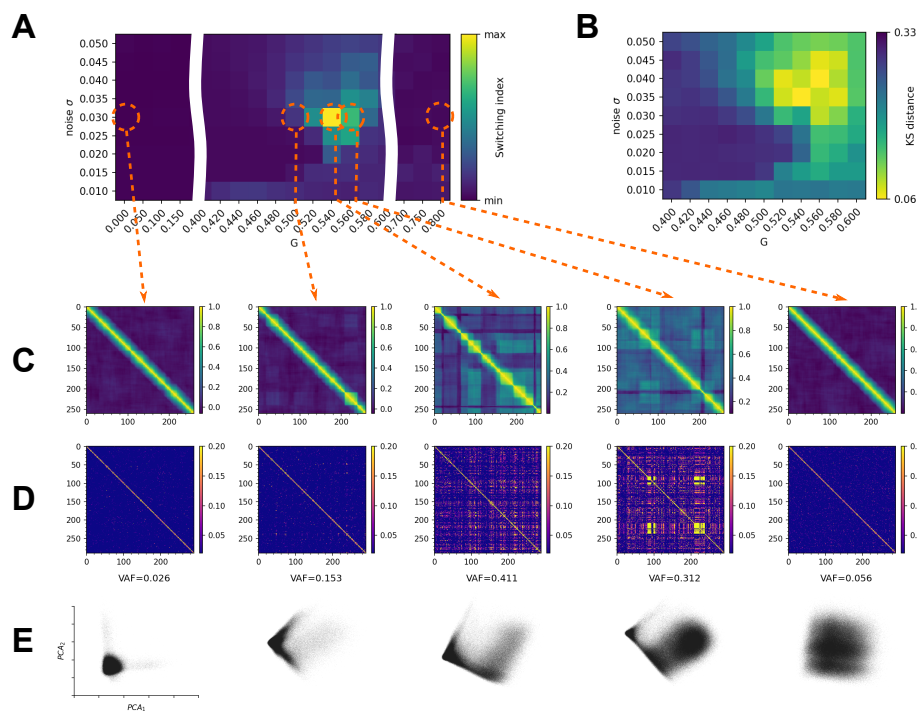
107 When driven by noise, the network of the bistable MPR nodes has the ca-
108 pacity to exhibit realistic dFC when the network input is scaled appropriately
109 [44]. The noise together with the network input drives the switching between
110 up- and down-state of the individual nodes, while the network mediates the co-
111 ordination reflected in the functional connectivity. In the following sections, we
112 explore how the manifold of the resting state activity arises from the networked
113 interactions, how it shapes the multistability of the functional connectivity in
114 the simulated BOLD, and how it relates to empirical observations.

115 2.1 Symmetry breaking: working point for dFC

116 To assess the impact of the symmetry breaking by the connectome, we simu-
117 lated 10 minutes of spontaneous activity for a range of values of the coupling
118 scaling parameter G and noise variance σ , and applied PCA to the source signal
119 $\Psi(t)$ and dFC to the BOLD (Figure 2). We used the variance accounted for
120 (VAF) of the first two PCA components as an estimate for the dimensionality
121 of the system’s dynamics in the state-space (Figure 2D), and the variance of the
122 upper triangle of the dFC matrix as a measure of the *fluidity* of the system’s
123 dynamics—that is the propensity to dwell in specific brain states (defined by the
124 functional connectivity) and shift and return between several such states (Fig-
125 ure 2A). In addition, using Kolmogorov-Smirnov distance between the centered
126 distributions of the values of the upper triangle of the dFC_w in the empirical
127 and simulated data, we have verified that the region of the parameter space
128 where dFC is most similar to the one derived from empirical data overlaps with
129 the region with the highest fluidity, Figure 2A.

130 For low values of G , the system exhibits high-dimensional dynamics as re-
131 flected in the low variance explained by the first PCA components and low
132 values of the variance of the off-diagonal values of dFC with the mean around
133 0—reflecting the absence of recurrence in the system dynamics (Figure 2B,C).
134 Note, that the explained variance for each PCA component is equal to $1/N$
135 (in this case $N = 84$ nodes of the network), and the projection in panel D
136 reflects the independent infrequent switching of two nodes, each captured by
137 one PCA component. Around the value of $G = G_w = 0.525$ and $\sigma_w = 0.030$
138 (working point) the variance explained by the first two components of the PCA

139 increases substantially, and so does the fluidity of the dFC as the characteristic
140 intervals of FC invariance (on-diagonal nonzero blocks) appear together with
141 similarity across time (high off-diagonal correlations). Past the working point
142 ($G > 0.6$) the explained variance in PCA drops as well as the off-diagonal dFC
143 correlations, signifying increase in dimensionality of the spontaneous dynamics.



144

145 **Figure 2: Brain network model and symmetry breaking.** The brain
 146 network model is simulated for varying levels of global coupling parameter G
 147 and noise variance σ to produce both time-series of the state space variables
 148 $\mathbf{r}(t)$, $\mathbf{V}(t)$, and the BOLD signal. For each combination of G and σ we compute
 149 the sliding window dFC_w matrix from the simulated BOLD signal, and quantify
 150 the "switching index" of the dFC as the variance of the upper triangle (A).
 151 Kolmogorov-Smirnov distance of the centered (mean-subtracted) distributions
 152 of the values of the upper triangle of the dFC computed from empirical and
 153 simulated resting state BOLD time series. The region of parameter space where
 154 the distributions are closest overlaps with the region with high fluidity of dFC
 155 (B). For selected values of (G, σ) we show the sliding window dFC_w (C), edge
 156 based dFC_e (D) and the projection of $\mathbf{r}(t)$ time series in the first two PCA
 157 components (E) annotated with corresponding fractional variance accounted
 158 for (VAF). In the working point around $G = 0.54$ and intermediate values of σ
 159 the system exhibits recurrence in the large-scale dynamics as captured by non-
 160 zero switching index, and reduction of dimensionality as captured in the increase
 161 in explained variance by the first PCA components and the asymmetry in the
 162 respective projection. For values of G below or above the working point, the
 163 systems loses the fluidity property as reflected in the absence of the off-diagonal
 164 blocks on the dFC, and exhibits high-dimensional dynamics.

165 2.2 Network dynamics

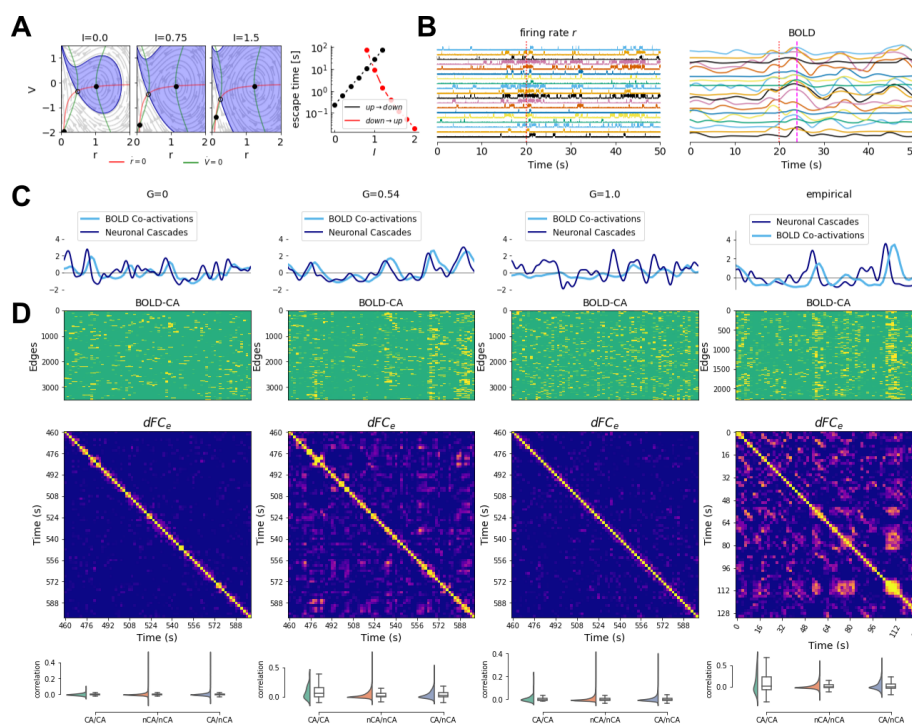
166 Before we delve into the characterization of the low-dimensional manifold, let
167 us first describe the network dynamics in detail. For the MPR model, the dy-
168 namical profile of an isolated node in the bistable parametrization consists of
169 an unstable fixed point (saddle node) and two stable fixed points: down-state
170 stable node and up-state focus (Figure 3A). Considering the uncoupled system,
171 that is, the joint dynamics of the N populations (nodes) in the absence of any
172 inter-population synaptic coupling, the phase flow is represented by 2^N stable
173 fixed points that contain all possible combinations of the populations firing at
174 either their low or high mean firing rates (down or up state, respectively). Start-
175 ing from an initial condition, the system will settle into the nearest accessible
176 such fixed point, a stable network state composed of a corresponding combina-
177 tion of regions in their up or down state. Thus, the dynamics of the uncoupled
178 system in phase space can be thought of as being driven by a potential energy
179 landscape with multiple stable local minima representing the stable attractor
180 states of the network. In fact, the uncoupled system, as such, is invariant under
181 permutation of the indexes of the populations, such that these latter attractor
182 network states are distinguished only in terms of the respective number of nodes
183 in up and down states. The global dynamics of the system, thus, collapses in
184 finite time onto this stable attractor state composed of a finite set of stable
185 equilibrium points that is invariant under shuffling of indexes of the nodes.
186 The associated global phase flow can be decomposed into N projections onto
187 the identical 2D phase planes of individual populations, depicted in Figure 3A.
188 Viewed from this perspective, the structure of the basins of attraction of the
189 2^N stable system equilibrium points redundantly inherits, in higher dimensions,
190 the relative structure of the basins of attraction of the two stable fixed points
191 of an individual population. For an isolated node, varying the external input
192 I_i changes the size of the basins of attraction of the stable fixed points. This
193 modulates the probability of switching between the two states when driven by
194 noise as captured by the mean escape times (Figure 3A, see Methods for more
195 detail). For a connected node, the external input I_e depends on the state of the
196 neighboring nodes (see Equation 4), fluctuating as they transition between the
197 up- and down-state. On the network level, given right scaling of the network
198 connections, this enables the cascades of up- and down-state switching at the
199 fast time-scale, and the co-fluctuation of the BOLD signal (Figure 3B).

200 To understand better the dynamical underpinning of the increase of fluidity
201 of the dFC we assess the characteristics of the co-fluctuations of the BOLD
202 signal and the cascades in the source signal. For the co-activations, we start
203 from the edge time series which is defined as pairwise dot product of z-scored
204 BOLD signal (an average over the edge time series would correspond to the
205 pearson correlation). The correlation across time-points yield the dFC_e matrix
206 capturing the recurrence of the edge configurations, and the root sum squared
207 (RSS) over the edges at each time point captures the contribution of that par-
208 ticular time point to the overall functional connectivity (see Methods for more
209 details). The time-points crossing the 95-th percentile threshold of the RSS are

210 considered as strong co-activation events. The neuronal cascades [44] are long
211 lasting perturbations of the neuroelectric activity and are measured on a global
212 level as a sum over regions of the binarized firing rate activity (at the threshold
213 of 3 standard deviations). We compared these measures between the working
214 point G_w , the disconnected system $G = 0$, the strong network coupling regime
215 $G \gg G_w$, and the empirical data (Figure 3C,D).

216 In the working point G_w the co-activations include large number of edges
217 (Figure 3D) and the RSS follows the number of cascades up to a short delay
218 corresponding to the delay of the BOLD signal. Moreover, some of the strong
219 co-activations re-occur partially in time as reflected in the non-zero elements
220 of the dFC_e matrix. The same profiles can be observed in the empirical data,
221 namely in the simultaneous EEG and fMRI recordings. On the other hand,
222 the characteristic spatial and temporal structure is lost outside of the working
223 point, that is either for the weakly coupled system ($G \ll G_w$), or for too strong
224 coupling ($G \gg G_w$).

225 To quantify how the co-activation events contribute to the characteristic
226 similarity across time, we compare the correlation of the edge vectors during the
227 events, during the non-events, and between events and non-events. As a result
228 we observe an increased similarity of the edge vectors during the events both in
229 the empirical data and in the simulations in the working point G_w . Again, this
230 property is lost for too weak ($G \ll G_w$) or for too strong coupling ($G \gg G_w$).
231 Together, these results show, that the system has a similar dynamical profile
232 in the working point G_w as observed in the empirical data with respect to the
233 network-carried fluctuations on both the fast and slow timescales (as captured
234 by dFC and cascades respectively).



235

236 **Figure 3: Network dynamics.** (A) The network input I modulates the
 237 probability of a noise-driven transition between the down- and up-state. (B)
 238 Example of a cascade—coordinated increase in activity translating to a delayed
 239 correlated peak in the BOLD signal. Below we compare the network dynamics
 240 in and outside the working point, and the empirical data. In both empirical
 241 data and the working point ($G = 0.54$), the BOLD co-activations follow the
 242 neuronal cascades with a latency (C), and show distinct spatial profiles which
 243 are recurrent in time (D): edge time series on the (top panel) captures the
 244 spatial profiles of the co-activations, the similarity across time is captured by
 245 the dFC_e matrix (middle panel), and the distributions of correlation between
 246 co-activation events (CA) and non-events (nCA) is compared (bottom panel).

247 2.3 Manifold of the resting state and characteristic sub- 248 spaces

249 Having characterized the dynamics of the system in the working point with an
 250 appropriate measure, we proceed with the description of the manifold on which
 251 it evolves—that is to show that this behavior is low-dimensional and constrained
 252 to a specific subspace. To relate cascades and co-activations to the trajectories
 253 of the system in the $2N$ -dimensional state space, we first select time intervals
 254 with similar functional connectivity. Starting from the edge time series for
 255 the magnitude of co-fluctuations, we clustered the time points using k-means

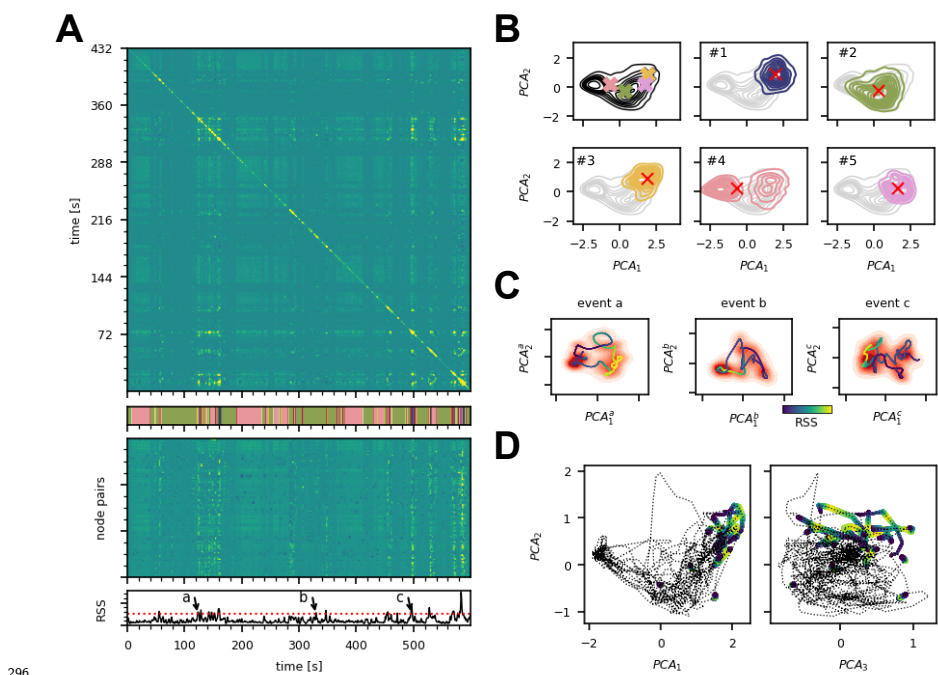
256 ($k=5$). This separated the high-activity intervals (majority of the nodes in the
257 up-state), low-activity intervals (majority of the nodes in the down-state), and
258 the co-fluctuation events (Figure 4A).

259 Next, we identified the trajectories of the system underlying each cluster
260 in the low dimensional projection of state space. For each cluster, we have
261 selected the corresponding time points in the state space of the system, and
262 projected them into the first two principal components of the PCA computed
263 on the complete time series. We have observed that while the corresponding
264 subspaces overlap partially in the projection (Figure 4B, colors correspond to
265 the clusters), the activity within the clusters concentrates to different subspaces.
266 This concentration in different subspaces is reflected in the distance between the
267 centroids of the cluster time points in the PCA projection.

268 While the cluster activity overlaps in the projection in the components of
269 the PCA computed from the whole time series, the co-activation trajectories be-
270 come clearer by choosing different basis to span the low-dimensional space, that
271 is, to compute the PCA from the time points corresponding to the individual
272 co-activation events. To project the trajectories of the events observed at the
273 slow time scale of the BOLD on the manifold, we have shifted the BOLD signal
274 by the characteristic lag, and for each BOLD time point belonging to the cluster
275 we selected the corresponding time points in $\mathbf{r}(t)$, and convolved the resulting
276 data with a Gaussian kernel to smoothen out the noisy fluctuations (see Meth-
277 ods for details). We then spanned the subspace corresponding to the first two
278 PCA components of the co-fluctuation trajectory and overlaid the smoothened
279 trajectory over the density plot of the full $\mathbf{r}(t)$ time series. The density plots
280 (shades of red, Figure 4C) of the example events show a separation of the event
281 subspace marked by the peak in the RSS (shown in yellow in Figure 4C) on
282 the smoothened trajectory from the rest of the manifold. This suggests that
283 the event subspace is relatively stable, allowing the system to dwell in it long
284 enough to cause the significant peaks in the slow BOLD signal, and that the
285 intermediate states are less stable than the event subspace or the rest of the
286 manifold and visited only transiently.

287 Although the linear embedding of the whole time-series does not separate
288 the event trajectories well when applied to the $\mathbf{r}(t)$ time series, the event trajec-
289 tories concentrate in the high-activity subspace spanned by the first two PCA
290 components of the BOLD signal (Figure 4D) .

291 Together, these results chart the low-dimensional manifold of the system in
292 the working point regime, associating the subspaces with specific flows. The
293 fluid dynamics as characterized in the previous section then arise from the slow
294 transitions between the low- and high-activity subspaces, where the latter sup-
295 ports the strong co-activation events which are reflected in the dFC .



296

297 **Figure 4: Manifold subspaces and characteristic dynamics.** (A) The
 298 edge-based dynamic functional connectivity dFC_e of a simulation of the model
 299 in the working point (top) shows the off-diagonal structure of similarity of the
 300 system's activity across time. The edge time series (middle) shows the time evolu-
 301 tion of the functional connectivity of the simulated BOLD signal between each
 302 of the node pairs, and exhibits the characteristic co-activation events defined as
 303 time points with the root sum squared (RSS, bottom) crossing the threshold of
 304 95th percentile. Dividing the edge-time series into 5 clusters (k-means, shown
 305 in the colorbar under the dFC) has separated the event and non-event time
 306 points, and also differentiated the events based on their respective similarity.
 307 (B) The time intervals in $\mathbf{r}(t)$ corresponding to the 5 clusters were selected; in
 308 the first panel the centroids of the time points of the individual clusters are
 309 marked with a cross in the projection to the first two principal components of
 310 the whole time series, following panels show the projection of the $\mathbf{r}(t)$ intervals
 311 of particular clusters. Cluster #2 captures the high-activity subspace, cluster #4
 312 corresponds to the low-activity state, and the clusters #1, #3, and #5 capture
 313 the co-activation events. (C) Local trajectories in the manifold subspaces: the
 314 time series of the three example events (a,b,c, marked in the panel A bottom)
 315 was projected to the first two components of PCA applied to each time seg-
 316 ment individually. The smoothened trajectory marks the advance of the system
 317 through the event and out of it, and is colored by the value of RSS (yellow at the
 318 peak of the event blue at the beginning and the end). (D) The event trajectories
 319 on the manifold. The trajectory of the simulated BOLD signal is projected in
 320 the space defined by the first three PCA components with the events colored
 321 by the RSS value (yellow at the peak of the event).

322 2.4 Fixed point skeleton and structured flow

323 To understand how the resting state manifold arises, we start by considering the
324 uncoupled system, that is, the joint dynamics of the N populations (nodes) in
325 the absence of any inter-population synaptic coupling. This uncoupled system's
326 phase flow is dominated by 2^N stable fixed points that represent all possible
327 combinations of the populations firing at either their low or high mean firing
328 rates (down or up state, respectively). Starting from an initial condition and
329 in the absence of noise, the BNM will settle into the nearest accessible such
330 fixed point, a stable network state composed of a corresponding combination of
331 regions in their up or down state.

332 The dynamical effects of the symmetry breaking in the BNM are delineated
333 by the topology of the connectome. The heterogeneity of the in-degree (to-
334 tal connectivity) of individual nodes of the network drives a variation in the
335 relative positioning of the separatrices between the basins of attraction of the
336 equilibrium points, mirrored in the variation of the corresponding projections
337 onto the 2D phase planes of corresponding nodes (see Figure 3A). In conjunc-
338 tion, connectivity strength and topology give rise to gradients in the relative
339 attractiveness of the system's equilibrium states. This attractiveness (or sta-
340 bility) can be quantified by the largest negative real eigenvalues obtained from
341 the linearization of the system about the respective equilibrium state (linear
342 stability analysis).

343 To map the complete manifold outside the simulated trajectories we sampled
344 the stable fixed points for varying coupling scaling parameter G from the 2^N
345 combinations of up- and down-states, and evaluated their stability (see Methods
346 for more details). We found that the number of stable fixed points in the sample
347 decreases with increasing G . This decrease is due to the loss of states with mixed
348 composition of up- and down-state due to the bifurcation of the down state in
349 nodes with high input (Figure 5A). Projecting the \mathbf{r} component of the fixed-
350 points in the first two eigenvectors of the Laplacian confirms this thinning of the
351 intermediate compositions biased towards those with higher number of nodes in
352 the up-state (corresponds to the first Laplacian eigenvector λ_1). Additionally,
353 the stability of the fixed points was inversely proportional to the number of
354 nodes in the up-state, that is in the direction of E_1 the first eigenvector of the
355 Laplacian (Figure 5B).

356 To put this into the context of the simulated trajectories, we have next iden-
357 tified the fixed points around which the simulated trajectory evolved by taking
358 initial conditions from the simulated trajectory, and integrating the system with-
359 out noise to the equilibrium. We have confirmed that in all instances the system
360 reached a stable fixed point composed of combination of up- and down-states,
361 and that the stability of these fixed points follows the same gradient in terms
362 of the composition (Figure 5C).

363 Furthermore, the nodes of the network exhibit a frequency gradient of the
364 oscillations in the up-state (Figure 5D). This gradient reflects variability of the
365 characteristic frequency in the up-state across nodes in the network. In the
366 fixed-point state, if the nodes are treated as isolated systems with an input

367 current term based on the existing network state, then

$$\begin{aligned} r_i^* &= r^* + \delta_i^r \\ v_i^* &= v^* + \delta_i^v \end{aligned} \quad (1)$$

368 where (r^*, v^*) are the symmetric fixed-points of the network and (δ_i^r, δ_i^v) are the
369 excursions from the symmetric fixed-point and change according to the existing
370 network state. These excursions depend directly on the in-strength of the i th
371 node and the local states of its first neighbours.

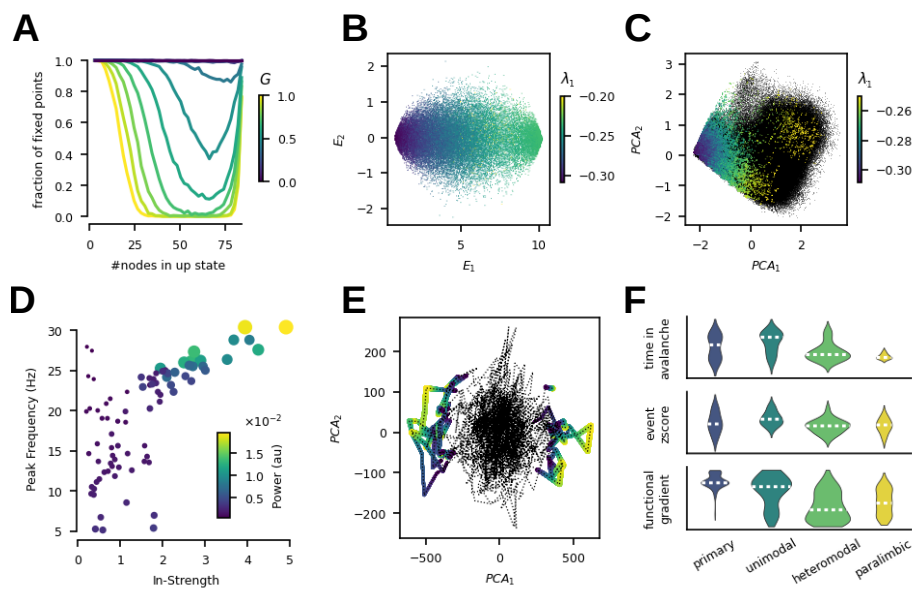
372 Following linear stability analysis of the i th system around the fixed-point
373 (see Methods), the eigenvalues of the Jacobian matrix are given by

$$\begin{aligned} \lambda_{1,2} &= 2v_i^* \pm \sqrt{Jr_i^* - 4\pi^2 r_i^{*2}} \\ &= 2v_i^* \pm \sqrt{2Jr_i^* - 4\pi^2 r_i^{*2} + 2J\delta_i^r - 4\pi^2 \delta_i^{r2} - 8\pi^2 r^* \delta_i^r} \end{aligned} \quad (2)$$

374 From the above equation, we see that the frequency of oscillations in the up-
375 state of the i th node increases proportional to δ_i^r and therefore proportional to
376 the in-strength of the node, which we also observe in the simulation (Figure 5D).

377 Furthermore, applying the PCA projection on the empirical BOLD time-
378 series, we have identified a similar separation of the event trajectories in the
379 global embedding as observed in the simulations (Figure 5E). However in the
380 case of the empirical data the system exhibits both the co-activations and co-
381 deactivations as seen on the separation through the first PCA component.

382 Lastly, symmetry breaking by the connectivity alone results in a spatial
383 organization of the above described flow which is aligned with empirically ob-
384 served trends (Figure 5F). In particular, per region the time spent in avalanches
385 and the cumulative z-scored BOLD signal within events both decrease across
386 the cortical hierarchy from the primary to paralimbic regions. The established
387 principal functional gradient extracted from the empirical fMRI data is also
388 aligned along this axis .



389

390 **Figure 5: Mechanistic structure of the manifold.** (A) Composition of
 391 the sampled stable fixed points in terms of number of nodes in the up-state as
 392 a function of G , normalized to $G = 0$. (B) Projection of the stable fixed points
 393 into the first two leading eigenmodes of the network Laplacian E_1, E_2 , color
 394 coded with the value of the largest eigenvalue in the linear stability analysis.
 395 (C) Fixed points (colored) derived by noise-free integration to equilibrium from
 396 the trace of a simulation (black) in the working point G_w , color coded by the
 397 value of the largest eigenvalue λ_1 . (D) Frequency peak in the simulated source
 398 activity of each of the regions plotted against the node structural connectivity
 399 in-strength. (E) Empirical BOLD time series projected into the first two PCA
 400 components with the events colored by the RSS value (yellow in the peak). (F)
 401 Across the cortical hierarchy, the time spent in avalanches of the $\mathbf{r}(t)$ time-
 402 series (top) decreases, as does the cumulative z-scored simulated BOLD from
 403 the event time-segments (middle). The spatial distribution of the principal
 404 functional gradient extracted from empirical fMRI is also aligned along the
 405 cortical hierarchy (bottom).

406 3 Discussion

407 Using a combination of computational modeling and dynamical systems analy-
 408 sis we have provided a complete mechanistic description in terms of constituent
 409 entities and their causal activities leading to spontaneous co-activations and
 410 neuronal cascades in the brain's resting state [44]. We showed how the breaking
 411 of the symmetry of the BNM's connectivity gives rise to the structured low-
 412 dimensional dynamics in the phase space and recurrent fluctuations of the func-

413 tional connectivity (Figure 2). These fluctuations arise from network-mediated
414 cascades of up- and down-state switching and capture well the empirically found
415 relationship between the strong co-activation events and the recurrence struc-
416 ture reflected by the functional connectivity dynamics (Figure 3). The subspace
417 accessible to the brain in this regime was charted and partitioned according to
418 the characteristic flow associated with each of the partition (Figure 4). Finally,
419 this subspace and its associated flows arise from the rich fixed point structure
420 of the system and the differential stability of the nodes in these fixed points is
421 not only reflected in the propensity to state switching that reflects the corti-
422 cal hierarchy, but also influences the dominant oscillation frequency (Figure 5).
423 In summary, these results support our hypothesis that the recurrent functional
424 connectivity states of the resting state correspond to distinct subspaces on a
425 low-dimensional manifold associated with distinct structured flows.

426 The central result of our work is that the symmetry breaking via the struc-
427 tural connectivity carves out an attractive subspace of all the possible states
428 of the brain, and that the flow on this manifold governs the characteristic dy-
429 namics of the brain (that is discarding the transient towards the manifold from
430 arbitrary initial conditions). In this regime, the model captures the multistabil-
431 ity and noise-driven exploration of the dynamic repertoire explored previously
432 in computational studies [2, 31, 32, 51, 52]. The data features extracted from
433 the time series provides a link between the empirical data and the model. Here,
434 the functional structure in the brain is carried by the rare high amplitude co-
435 fluctuation events as it was previously demonstrated in empirical fMRI data [19,
436 21, 53], and in simultaneous EEG and fMRI measurements [44]. Similarly, re-
437 cent modeling study has shown the role of structural modules of the network in
438 shaping the co-fluctuation events [54], which is aligned with the brain network
439 as the symmetry breaking gives rise to the low-dimensional dynamics.

440 The slow time scale fluctuations of the dynamical functional connectivity
441 reflect the movement of the brain activity between the low- and high-activity
442 subspaces of the manifold. The flow in the high-activity subspace supports
443 the cascades, which in turn are reflected in the high activity coactivations. This
444 movement points to the multistable rather than metastable interpretation of the
445 resting state dynamics [55], and reflects the observation of switching between a
446 low-amplitude incoherent and high-amplitude coherent states in empirical data
447 [56]. Furthermore, the slow transitions between the high- and low-activity sub-
448 spaces is compatible with the reports on the spontaneous infra-slow brain ac-
449 tivity [57, 58] and the detailed reports on its spatio-temporal structure. For
450 example, the slow traveling waves [22] propagating along the principal gradi-
451 ent of cortical organization [59, 60] would provide a refined description of the
452 trajectory through the manifold subspaces.

453 The attractive subspace of the low-dimensional manifold and the associated
454 structured flow arise in the presented system from the changes in the fixed-
455 point structure due to the irregular connectivity. In particular, the network
456 input mediates the modulation of the escape times of the noise-induced transi-
457 tions. These chain into domino-like sequences [61, 62], which in turn constitute
458 the neuronal cascades. On a network level, our results elaborate the previous

459 analytical results of increased entropy of the attractors in an Ising-spin network
460 model for intermediate values of coupling strength [63]. The relationship to
461 the dimensionality of the exhibited dynamics is such that for the low values of
462 coupling strength G , where the Ising model is in the trivial state with all spins
463 equal to 0, the model presented here is also driven by noise to the all-down
464 state due to the significantly larger basin of attraction of the down-state, and
465 the nodes make uncoordinated noise-driven excursions to the up-state reflected
466 in the high-dimensionality of the dynamics. For high values of G the situation is
467 opposite, and for intermediate values of G the Ising model exhibits high entropy
468 of attractors, which is in our case reflected in the available states organized in
469 the low-dimensional manifold with the structured flow governed by the stability
470 of these states.

471 Overall, the movement of the system through the subspaces of a low-dimensional
472 manifold is in accordance with empirical and modeling results on recurrence and
473 state clustering of resting state fMRI BOLD recordings. Using clustering algo-
474 rithms to partition the BOLD time series yields statistically similar and tempo-
475 rally recurrent whole brain spatial coactivation patterns [18, 45] associated
476 with specific dwell times and transition probabilities. However, compared to the
477 clustering approaches applied to the BOLD time-series, the SFMs allows us to
478 refine the partitioning of the state-space in two aspects: we unfold the subspaces
479 based on the similarity of the coactivations on the level of the BOLD signal, and
480 we provide a detailed description of the flow of the system in these subspaces
481 e.g. in terms of the cascades. The former is in line with the recent advances
482 regarding the low-dimensional representation of meso- [64, 65] and macroscopic
483 [66, 67] brain dynamics, but the latter describes the origin of those subspaces
484 as constrained by the connectome. Interestingly, the clustering of phase-locking
485 BOLD states [43] leads to very similar low-dimensional representation of the
486 resting state dynamics to our approach, with a single dominant global phase
487 locked state and a number of transient partially phase-locked states related to
488 functional networks. Similarly, by embedding the resting state data onto the
489 task manifold extracted with the help of diffusion maps, [68] found that rest-
490 ing state time-points concentrate in the task-fixation and transition subspaces,
491 and only a minority of time-points reach to the cognitive subspaces of the task
492 manifold.

493 The description of the structured flow addresses also the fast time-scale by in-
494 cluding the cascades, which we previously showed to relate to the co-activations
495 observed in the BOLD signal [44]. In EEG literature, the spatio-temporal struc-
496 ture of the resting state dynamics is characterized with the help of microstates—
497 sensor-level transient patterns lasting on average for 60-150 ms [69]. Attempts
498 have been made to relate the microstates to BOLD activation clusters [70, 71],
499 but identifying the sources generating the microstates with clustering or regres-
500 sion analysis has been challenging so far due to unclear relationship between the
501 broadband EEG activity and the BOLD signal fluctuations [72]. To advance
502 we propose to reframe the question as a search for a shared manifold of the
503 neuronal activity with specific slow and fast time-scale characteristics which in
504 turn are reflected in the EEG and the BOLD observables.

505 The manifold we describe is conceptually reminiscent of energy landscapes
506 described in previous works [40, 41]. However, previous energy landscape mod-
507 els, such as in [41], implicitly assume energy minimization and thus, by con-
508 struction, encode the hypothesis that the activation of two brain regions that
509 are connected via a direct structural connection is more energetically favorable
510 than that of two regions that are not directly connected. We make no such
511 assumption here and, instead, the effective energy landscape emerges, in the
512 form of a low dimensional manifold, out of the interplay of the non-linearity in
513 the local neural mass model and the connectome, thus fully embracing the the
514 network impact, beyond the pair-wise interactions. In addition, previous en-
515 ergy landscape analysis [40] assumed that the network changes only gradually
516 by flipping one region at a time, and did not account for transitions in which
517 several regions flip simultaneously. Treating the brain as a whole, the BNM
518 that we presented here instead allows for such latter transitions of the system
519 in state space, which may very well be due to strongly connected regions that
520 are able to simultaneously influence their nearest neighbors during coactivation
521 events.

522 It is worth pointing that our framework covers only one part of the mecha-
523 nisms that shape the brain’s manifold and the flow on it, that is the connectome.
524 We have assumed identical parameters for each region, ignoring the known struc-
525 tural hierarchies [73], which have been shown to improve the predictive value of
526 the BNMs [56, 74, 75]. While we observed differential functional properties of
527 the nodes across the cortical hierarchy [76], we didn’t recover the exact spatial
528 correspondence to the established functional gradients [59]. Neuromodulation
529 and the subcortical drives [77] are another missing aspect that similarly improve
530 the performance of BNMs [78]. However, both of these elements are not yet es-
531 tablished in the framework of BNMs, as is the impact of the connectome [24].
532 Thus our goal here is not to generate *in silico* observables that are as close as
533 possible to the empirical one, which nevertheless differ a lot depending on the
534 preprocessing, e.g. see [79], but to focus on the generative mechanisms for the
535 key data features across time-scales and neuroimaging modalities that render
536 functional activity identifiable across subjects [12, 13, 80].

537 A natural next step will be to extend the analysis to include the impact
538 of the data-informed regional variance [81] which is now reachable by TVB
539 through Ebrains [82]. Similarly intriguing direction for the extension of the
540 framework presented here is in more refined inclusion of the subcortical struc-
541 tures, especially their impact through the neuromodulation. Notably, recent
542 works [77, 83, 84] exploring the role of thalamus, locus coeruleus, and basal nu-
543 cleus of Meynert in shaping of the dynamical landscape of the cortical activity
544 are already formulated in the dynamical systems language while incorporating
545 carefully the detailed anatomical and cytoarchitectural knowledge. Integrating
546 these advances in the SFM framework is a natural next step towards the origi-
547 nal motivation of SFM, that is to link the mesoscopic neuronal activity to the
548 behaviour, as the intricate interactions between cortex and the subcortical areas
549 are one of the organizing principles of the underlying the biological mechanisms
550 supporting behaviour [85].

551 Parcellation-induced variation of empirical and simulated brain connectomes
552 at group and subject levels is another issue that needs to be considered [86].
553 Nevertheless, we focus on general mechanisms without going on regional level
554 specificities, so the choice of parcellation should not play such a role.

555 In conclusion, our results show how the low-dimensional dynamics arises
556 from breaking the symmetry in the brain on the level of the connectome. De-
557 scribing these dynamics as structured flows on manifolds allows us to bridge the
558 gap between the observational measures and the state-space trajectories of the
559 system. As such, this object is well suited for comparison across different mod-
560 els, scales, and neuroimaging modalities, and provides means for integration of
561 the diverse descriptions of the resting state dynamics.

562 4 Materials and methods

563 4.1 Brain network model

564 Computational brain network model [87] is used to simulate resting state activity
565 under varying values of network coupling scaling parameter G . The dynamics
566 of each of the network nodes were governed by the neural mass model (NMM)
567 derived analytically as the limit of infinitely all-to-all coupled θ -neurons [48],
568 namely for i -th node for the firing rate r_i and membrane potential v_i as:

$$\begin{aligned}\tau_c \dot{r}_i &= \frac{\Delta}{\pi \tau_c} + 2r_i v_i, \\ \tau_c \dot{v}_i &= v_i^2 + \eta - (\tau_c \pi r_i)^2 + J \tau_c r_i + I_i,\end{aligned}\tag{3}$$

569 where I_i is the input current, η is the average neuronal excitability, J is the
570 synaptic weight, Δ is the spread of heterogeneous noise distribution, and τ_c
571 is the characteristic time.

572 The N nodes are then coupled with a connectome derived from empirical
573 data as

$$I_i(t) = G \sum_j W_{ij} r_j(t - D_{ij}),\tag{4}$$

574 where G is the network scaling parameter, W_{ij} is the connection weight, $D_{ij} =$
575 L_{ij}/S is the delay caused by propagation of the signal on a tract of length
576 L_{ij} with finite speed S . We picked the speed $S = 2m/s$ from the biologically
577 plausible range [88], and a connectivity matrix of a subject from the Human
578 Connectome Project [49] in the Desikan-Killiany parcellation [89] with 84 regions
579 including subcortical structures.

580 The equations 3 and 4 comprise the drift $a(\Psi, t)$ in the stochastic delay
581 differential equation formulation with linear additive noise reading:

$$d\Psi(t) = a(\Psi(t))dt + b(\Psi(t))dW(t),\tag{5}$$

582 where Ψ is the state vector $[\psi_1, \dots, \psi_n]$ with $\psi_n = [r_n, V_n]$, $dW(t)$ is a differential
583 of a Wiener process with Gaussian increment with variance σ^2 , and $b(\Psi, t) = 1$
584 is the diffusion coefficient—here constant yielding the noise term additive.

585 The model was implemented in The Virtual Brain [47] and equipped with
 586 BOLD forward solution comprising the Balloon-Windkessel model applied to
 587 the firing rate $\mathbf{r}(t)$ [50].

588 The model parameters $\eta = -5.0$, $J = 15.0$, $\tau_c = 1.0$, and $\Delta = 1.0$ were
 589 selected to set the nodes in the bi-stable regime in the absence of coupling [48].
 590 We then varied the global coupling parameter G and the noise variance σ , and
 591 simulated 10 minutes of resting state BOLD activity with $TR = 720ms$ after
 592 discarding 10 seconds of the initial transient from random initial conditions.

593 4.2 Functional connectivity dynamics

594 In order to track the time-dependent changes in the functional connectivity, we
 595 compute the windowed dynamical functional connectivity dFC_w [32, 90] and
 596 edge dynamical functional connectivity dFC_e [44]. Starting from the regional
 597 BOLD time-series $B_n(t)$ for each node n , we compute functional connectivity
 598 matrices $FC(w)$ for each time window $w = 1 \dots W$ defined as $B_n(t)|_{t_w}^{t_w + \tau}$ with
 599 window length $\tau = 60s$ and window step size $t_{(w+1)} - t_w = 2s$. Next we compute
 600 the dFC_w matrix of order W as

$$dFC_w(i, j) = \text{corr}(FC(w_i)^\Delta, FC(w_j)^\Delta), \quad (6)$$

601 where $FC(w)^\Delta$ is the vectorized upper part of the FC matrix.

602 For the window-less dFC_e [44] we start from the edge time-series [21] defined
 603 as $E_{nm}(t) = z_n(t)z_m(t)$ for $n, m = 1 \dots N$ where $z_n(t) = \frac{B_n - \mu_n}{\sigma_n}$ is the z-scored
 604 BOLD time-series of a node n . The edge dynamical functional connectivity
 605 is then computed as correlation between the edge vectors at each pair of time
 606 points t_1, t_2 :

$$dFC_e(t_1, t_2) = \text{corr}(E_{nm}(t_1), E_{nm}(t_2)). \quad (7)$$

607 The co-fluctuation events (CF) are defined as time points in the edge time-
 608 series $E_{nm}(t)$ during which the root sum squared $RSS = \sqrt{\sum_{nm} E_{nm}^2(t)}$ crosses
 609 a given threshold, here chosen as 95th percentile. Time points where RSS is
 610 below the threshold are then labeled as non-events (nCF).

611 The avalanches were computed on the binary mask $\mathbf{a}(t)$ on the $\mathbf{r}(t)$ such
 612 that $a_i(t) = 1 \iff z(r_i(t)) > 3$ where $z(r_i(t))$ is the z-score of firing rate r of a
 613 node i .

614 4.3 Manifold subspaces

615 As a first step in the analysis of the local dynamics specific to a particular
 616 attractive subspace, we have extracted the time-points belonging to these sub-
 617 spaces with k-means clustering applied to the edge time series $E_{nm}(t)$. We
 618 varied the number of clusters k and selected $k = 5$ at which the co-fluctuation
 619 events separated to distinct cluster.

620 To extract the segments of $\mathbf{r}(t)$ corresponding to the $E_{nm}(t)$ time points
 621 we first estimated the BOLD signal lag $l = 2500ms$ as optimal peak-to-peak

622 alignment with $\mathbf{r}(t)$ smoothed by a Gaussian filter with same effective width
 623 ($\sigma = 700$). Then for all BOLD time points in a given cluster c we selected the
 624 2000 corresponding time points in $\mathbf{r}(t)$ and concatenate these to get the fast
 625 time-scale activity $\mathbf{r}_c(t)$ in the subspace corresponding to cluster c . Each of the
 626 $\mathbf{r}_c(t)$ was then projected to space spanned by the first two PCA components
 627 of the whole $\mathbf{r}(t)$ time-series to evaluate how much of the overall state-space is
 628 covered by individual clusters.

629 The local trajectory for a given event e was computed by selecting interval
 630 $\mathbf{r}_e(t)$ corresponding to BOLD timepoints above the RSS threshold and three
 631 timepoints before and after the event. Local PCA^e of was then computed from
 632 $\mathbf{r}_e(t)$, and the smoothed trajectory was computed by convolving $\mathbf{r}_e(t)$ with a
 633 Gaussian filter ($\sigma = 100$).

634 4.4 Manifold sampling

635 To identify the fixed point scaffold of the manifold as traced by the trajectory
 636 resulting from integrating the Equation 5, we sample the segments from the
 637 simulated trajectory $(r_i(t), v_i(t))|_{t_s}^{t_s + \tau_{max}}$, and use them as initial conditions
 638 for integration of the deterministic interpretation of Equation 5, i.e. $d\Psi(t) =$
 639 $a(\Psi(t))dt$. From each such an initial condition, we integrated the system to
 640 steady state equilibrium corresponding to a fixed point $(\mathbf{r}^*, \mathbf{v}^*)$.

641 The number of stable fixed points $(\mathbf{r}^*, \mathbf{v}^*)$ of system with $G = 0$ is 2^N
 642 reflecting all the combinations of up- and down-states of the N nodes. To
 643 sample the stable fixed points of the system with $G > 0$ we solve repeatedly the
 644 system of equations:

$$\begin{aligned} 0 &= \frac{\Delta}{\pi\tau_c} + 2r_i^*v_i^*, \\ 0 &= v_i^{*2} + \eta - (\tau_c\pi r_i^*)^2 + J\tau_c r_i^* + I_i \end{aligned} \quad (8)$$

645 using Newton-Raphson method with the initial conditions chosen randomly as a
 646 vector of up- and down-state fixed points of the isolated nodes, i.e. $(r_i^{*0}, v_i^{*0}) \in$
 647 $\{(r_\uparrow^*, v_\uparrow^*), (r_\downarrow^*, v_\downarrow^*)\}$, $\forall i$ where $(r_\uparrow^*, v_\uparrow^*)$ and $(r_\downarrow^*, v_\downarrow^*)$ are the up- and down-state fixed
 648 points for the isolated node. For each initial condition $(\mathbf{r}^{*0}, \mathbf{v}^{*0})$ we then check
 649 if the corresponding solution of Equation 8 is equivalent up to the composition
 650 in terms of up- and down-states. If not, it is discarded, otherwise we evaluate
 651 the stability of the found fixed point using linear stability analysis.

652 As a low-dimensional projection of the sampled manifold we have used the
 653 two slowest eigenmodes of the structural connectivity. These are computed as
 654 eigendecomposition of the graph Laplacian $\mathbf{L} = \mathbf{W} - \mathbf{I}$, that is $\mathbf{L}\mathbf{U} = \mathbf{U}\mathbf{\Lambda}$, where
 655 eigenvalues λ_k can be interpreted as structural frequencies and the eigenmodes
 656 \mathbf{u}_k as structural connectome harmonics [91].

657 4.5 Linear stability analysis

658 We perform a linear stability analysis to identify the fixed-points obtained from
 659 the NR method. If each fixed-point $(\mathbf{r}^*, \mathbf{v}^*)$ is perturbed by (ϵ^r, ϵ^v) , then the

660 evolution of the perturbations depend on the Jacobian matrix (J) and are given
 661 by:

$$\begin{bmatrix} \dot{\epsilon}_1^r \\ \dot{\epsilon}_2^r \\ \vdots \\ \dot{\epsilon}_N^r \\ \dot{\epsilon}_1^v \\ \dot{\epsilon}_2^v \\ \vdots \\ \dot{\epsilon}_N^v \end{bmatrix} = \begin{bmatrix} 2v_1^* & 0 & \dots & 0 & 2r_1^* & 0 & \dots & 0 \\ 0 & 2v_2^* & \dots & 0 & 0 & 2r_2^* & \dots & 0 \\ \vdots & \vdots & \ddots & \vdots & \vdots & \vdots & \ddots & \vdots \\ 0 & 0 & \dots & 2v_N^* & 0 & 0 & \dots & 2v_N^* \\ J - 2\pi^2 r_1^* & w_{12} & \dots & w_{1N} & 2v_1^* & 0 & \dots & 0 \\ w_{21} & J - 2\pi^2 r_2^* & \dots & w_{2N} & 0 & 2v_2^* & \dots & 0 \\ \vdots & \vdots & \ddots & \vdots & \vdots & \vdots & \ddots & \vdots \\ w_{N1} & w_{N2} & \dots & J - 2\pi^2 r_N^* & 0 & 0 & \dots & 2v_N^* \end{bmatrix} \cdot \begin{bmatrix} \epsilon_1^r \\ \epsilon_2^r \\ \vdots \\ \epsilon_N^r \\ \epsilon_1^v \\ \epsilon_2^v \\ \vdots \\ \epsilon_N^v \end{bmatrix} \quad (9)$$

662 The stability of a fixed-point depends on the eigenvalues of the Jacobian evalu-
 663 ated at the fixed-point. The fixed-point is stable iff all the eigen-values of J are
 664 negative. Therefore, we numerically evaluate the largest eigenvalue of Jacobian
 665 for each fixed-point and label the point as stable if its real-part is negative.

666 4.6 Fixed point sampling from simulated trajectory

667 From a given trajectory of the system given as 10 minutes of $\psi(t)$ we have
 668 selected a restart point t' each 50 ms (12000 starting points altogether). For
 669 each of the restart point t' we extracted the segment $\Psi(t)|_{t'}^{t'-\tau_{max}}$ where τ_{max}
 670 is the length of the longest delay, and used as initial condition to a equivalent
 671 system to Equation 5 with $b = 0$:

$$d\Psi(t) = a(\Psi(t))dt. \quad (10)$$

672 Integrating this system to equilibrium yielded then for each restart point t_r a
 673 fixed point $\Psi^* = (\mathbf{r}^*, \mathbf{v}^*)$. The stability of each of the fixed points Ψ^* was
 674 then evaluated using the linear stability analysis as the largest eigenvalue of the
 675 respective Jacobian matrix.

676 4.7 Escape time analysis

677 The switching behaviour of a single node is driven by the stability of the up-
 678 and down-state fixed points in the presence of noise. We employed escape time
 679 analysis [92] to measure the stability of these fixed points for range of values of
 680 external input I . In detail, for a single node of the system given by Equation 3
 681 we found the up- and down-state stable fixed points $(r^*, v^*)^\uparrow$ and $(r^*, v^*)^\downarrow$, and
 682 the unstable saddle node $(r^*, v^*)^\times$. Next we computed the separatrix between
 683 the two basins of attraction by integration of the model backwards in time
 684 resulting in an closed curve ω . To find the characteristic escape time for a
 685 fixed point (r^*, v^*) we have integrated the system from the initial condition
 686 $(r_0, v_0) = (r^*, v^*)$ for a given value of I 100 times, measuring the time t_E at
 687 which the trajectory crosses ω for the first time. The values of I were drawn

688 from the range given by $[0, I_{\max}]$ where $I_{\max} = \max\{I_i(t), \forall i\}$ is the largest value
689 of I_i encountered in the integration of the full system in the working point.

690 4.8 Empirical data and spatial analysis

691 The functional gradient on empirical data was computed from the group connectiv-
692 ity matrix of the Human Connectome Project dataset using the brainspace
693 toolbox [93]. For a simulated resting state session with G_w , the time in avalanche
694 was computed for each node as total time for which the $\mathbf{r}_i(t)$ was above the
695 threshold of 3 standard deviations, and the event z-score as a sum of z-scored
696 BOLD signal in time-points marked as events. The nodes were then grouped
697 according to the cortical hierarchy [76] projected to the Desikan-Killiany par-
698 cellation.

699 A parcellation-based BOLD signals of a resting-state session from a subject
700 from the Human Connectome Project [94] were used to validate the separation
701 of the events in the low-dimensional embedding. The data consisted of 1200
702 time points sampled at 720 ms in the Desikan-Killiany parcellation [89] with 70
703 cortical regions.

704 References

- 705 1. Honey, C. J., Kötter, R., Breakspear, M. & Sporns, O. Network structure
706 of cerebral cortex shapes functional connectivity on multiple time scales.
707 en. *Proc. Natl. Acad. Sci. U. S. A.* **104**, 10240–10245. ISSN: 0027-8424
708 (June 2007).
- 709 2. Ghosh, A., Rho, Y., McIntosh, A. R., Kötter, R & Jirsa, V. K. Noise during
710 rest enables the exploration of the brain’s dynamic repertoire. en. *PLoS*
711 *Comput. Biol.* **4**, e1000196. ISSN: 1553-734X, 1553-7358 (Oct. 2008).
- 712 3. Deco, G., Jirsa, V. K. & McIntosh, A. R. Resting brains never rest: compu-
713 tational insights into potential cognitive architectures. en. *Trends Neurosci.*
714 **36**, 268–274. ISSN: 0166-2236, 1878-108X (May 2013).
- 715 4. Cabral, J., Kringelbach, M. L. & Deco, G. Functional connectivity dynam-
716 ically evolves on multiple time-scales over a static structural connectome:
717 Models and mechanisms. en. *Neuroimage* **160**, 84–96. ISSN: 1053-8119,
718 1095-9572 (Oct. 2017).
- 719 5. Gusnard, D. A., Raichle, M. E. & Raichle, M. E. Searching for a baseline:
720 functional imaging and the resting human brain. en. *Nat. Rev. Neurosci.*
721 **2**, 685–694. ISSN: 1471-003X (Oct. 2001).
- 722 6. Damoiseaux, J. S. *et al.* Consistent resting-state networks across healthy
723 subjects. en. *Proc. Natl. Acad. Sci. U. S. A.* **103**, 13848–13853. ISSN: 0027-
724 8424 (Sept. 2006).
- 725 7. Deco, G., Jirsa, V. K. & McIntosh, A. R. Emerging concepts for the dyn-
726 amical organization of resting-state activity in the brain. en. *Nat. Rev.*
727 *Neurosci.* **12**, 43–56. ISSN: 1471-003X, 1471-0048 (Jan. 2011).

- 728 8. Hutchison, R. M. *et al.* Dynamic functional connectivity: promise, issues,
729 and interpretations. en. *Neuroimage* **80**, 360–378. ISSN: 1053-8119, 1095-
730 9572 (Oct. 2013).
- 731 9. Preti, M. G., Bolton, T. A. & Van De Ville, D. The dynamic functional
732 connectome: State-of-the-art and perspectives. en. *Neuroimage* **160**, 41–
733 54. ISSN: 1053-8119, 1095-9572 (Oct. 2017).
- 734 10. Shine, J. M. *et al.* The Dynamics of Functional Brain Networks: Integrated
735 Network States during Cognitive Task Performance. en. *Neuron* **92**, 544–
736 554. ISSN: 0896-6273, 1097-4199 (Oct. 2016).
- 737 11. Cavanna, F., Vilas, M. G., Palmucci, M. & Tagliazucchi, E. Dynamic
738 functional connectivity and brain metastability during altered states of
739 consciousness. en. *Neuroimage* **180**, 383–395. ISSN: 1053-8119, 1095-9572
740 (Oct. 2018).
- 741 12. Battaglia, D. *et al.* Dynamic Functional Connectivity between order and
742 randomness and its evolution across the human adult lifespan. en. *Neu-
743 roimage* **222**, 117156. ISSN: 1053-8119, 1095-9572 (Nov. 2020).
- 744 13. Petkoski, S., Ritter, P. & Jirsa, V. K. White-matter degradation and dy-
745 namical compensation support age-related functional alterations in human
746 brain. *Cerebral Cortex* **bhac500**, 1–16 (2023).
- 747 14. Braun, U. *et al.* From Maps to Multi-dimensional Network Mechanisms of
748 Mental Disorders. en. *Neuron* **97**, 14–31. ISSN: 0896-6273, 1097-4199 (Jan.
749 2018).
- 750 15. Jones, D. T. *et al.* Non-stationarity in the "resting brain's" modular archi-
751 tecture. en. *PLoS One* **7**, e39731. ISSN: 1932-6203 (June 2012).
- 752 16. Zalesky, A., Fornito, A., Cocchi, L., Gollo, L. L. & Breakspear, M. Time-
753 resolved resting-state brain networks. en. *Proc. Natl. Acad. Sci. U. S. A.*
754 **111**, 10341–10346. ISSN: 0027-8424, 1091-6490 (July 2014).
- 755 17. Baker, A. P. *et al.* Fast transient networks in spontaneous human brain
756 activity. en. *Elife* **3**, e01867. ISSN: 2050-084X (Mar. 2014).
- 757 18. Beim Graben, P. *et al.* Metastable Resting State Brain Dynamics. *Frontiers
758 in Computational Neuroscience* **13** (2019).
- 759 19. Tagliazucchi, E., Balenzuela, P., Fraiman, D. & Chialvo, D. R. Critical-
760 ity in large-scale brain fMRI dynamics unveiled by a novel point process
761 analysis. en. *Front. Physiol.* **3**, 15. ISSN: 1664-042X (Feb. 2012).
- 762 20. Liu, X., Zhang, N., Chang, C. & Duyn, J. H. Co-activation patterns in
763 resting-state fMRI signals. en. *Neuroimage* **180**, 485–494. ISSN: 1053-8119,
764 1095-9572 (Oct. 2018).
- 765 21. Esfahlani, F. Z. *et al.* High-amplitude co-fluctuations in cortical activity
766 drive functional connectivity. en. *Proc. Natl. Acad. Sci. U. S. A.* **117**,
767 28393–28401. ISSN: 0027-8424, 1091-6490 (Nov. 2020).

- 768 22. Gu, Y. *et al.* Brain Activity Fluctuations Propagate as Waves Traversing
769 the Cortical Hierarchy. en. *Cereb. Cortex* **31**, 3986–4005. ISSN: 1047-3211,
770 1460-2199 (July 2021).
- 771 23. Mišić, B. *et al.* Network-Level Structure-Function Relationships in Human
772 Neocortex. en. *Cereb. Cortex* **26**, 3285–3296. ISSN: 1047-3211, 1460-2199
773 (July 2016).
- 774 24. Breakspear, M. Dynamic models of large-scale brain activity. en. *Nat. Neu-*
775 *rosci.* **20**, 340–352. ISSN: 1097-6256, 1546-1726 (Feb. 2017).
- 776 25. O’Byrne, J. & Jerbi, K. How critical is brain criticality? *Trends in Neuro-*
777 *sciences* (2022).
- 778 26. Deco, G., Jirsa, V., McIntosh, A. R., Sporns, O. & Kötter, R. Key role
779 of coupling, delay, and noise in resting brain fluctuations. en. *Proc. Natl.*
780 *Acad. Sci. U. S. A.* **106**, 10302–10307. ISSN: 0027-8424, 1091-6490 (June
781 2009).
- 782 27. Deco, G. *et al.* Dynamical consequences of regional heterogeneity in the
783 brain’s transcriptional landscape. en. *Sci. Adv.* **7**, eabf4752. ISSN: 2375-
784 2548 (July 2021).
- 785 28. Melozzi, F. *et al.* Individual structural features constrain the mouse func-
786 tional connectome. en. *Proc. Natl. Acad. Sci. U. S. A.* ISSN: 0027-8424,
787 1091-6490 (Dec. 2019).
- 788 29. Shine, J. M. *et al.* *The dynamic basis of cognition: an integrative core under*
789 *the control of the ascending neuromodulatory system* en. May 2018.
- 790 30. Roberts, J. A. *et al.* Metastable brain waves. en. *Nat. Commun.* **10**, 1056.
791 ISSN: 2041-1723 (Mar. 2019).
- 792 31. Courtiol, J., Guye, M., Bartolomei, F., Petkoski, S. & Jirsa, V. K. Dy-
793 namical mechanisms of interictal resting-state functional connectivity in
794 epilepsy. *Journal of Neuroscience* **40**, 5572–5588. ISSN: 15292401 (2020).
- 795 32. Hansen, E. C. A., Battaglia, D., Spiegler, A., Deco, G. & Jirsa, V. K.
796 Functional connectivity dynamics: modeling the switching behavior of the
797 resting state. en. *Neuroimage* **105**, 525–535. ISSN: 1053-8119, 1095-9572
798 (Jan. 2015).
- 799 33. Machamer, P., Darden, L. & Craver, C. F. Thinking about mechanisms.
800 *Philosophy of science* **67**, 1–25 (2000).
- 801 34. Jirsa, V. in *Selbstorganisation—ein Paradigma für die Humanwissenschaften*
802 89–102 (Springer, 2020).
- 803 35. Pillai, A. S. & Jirsa, V. K. Symmetry Breaking in Space-Time Hierarchies
804 Shapes Brain Dynamics and Behavior. *Neuron* **94**, 1010–1026 (2017).
- 805 36. Huys, R., Perdikis, D. & Jirsa, V. K. Functional architectures and struc-
806 tured flows on manifolds: a dynamical framework for motor behavior. en.
807 *Psychol. Rev.* **121**, 302–336. ISSN: 0033-295X, 1939-1471 (July 2014).

- 808 37. McIntosh, A. R. & Jirsa, V. K. The hidden repertoire of brain dynamics
809 and dysfunction. en. *Netw Neurosci* **3**, 994–1008. ISSN: 2472-1751 (Sept.
810 2019).
- 811 38. Woodman, M. M. & Jirsa, V. K. Emergent dynamics from spiking neuron
812 networks through symmetry breaking of connectivity. *PloS one* **8**, e64339
813 (2013).
- 814 39. Watanabe, T. *et al.* A pairwise maximum entropy model accurately de-
815 scribes resting-state human brain networks. *Nature communications* **4**, 1–
816 10 (2013).
- 817 40. Watanabe, T. *et al.* Energy landscapes of resting-state brain networks. en.
818 *Front. Neuroinform.* **8**, 12. ISSN: 1662-5196 (Feb. 2014).
- 819 41. Gu, S. *et al.* The Energy Landscape of Neurophysiological Activity Implicit
820 in Brain Network Structure. en. *Sci. Rep.* **8**, 2507. ISSN: 2045-2322 (Feb.
821 2018).
- 822 42. Ashourvan, A., Gu, S., Mattar, M. G., Vettel, J. M. & Bassett, D. S.
823 The energy landscape underpinning module dynamics in the human brain
824 connectome. *Neuroimage* **157**, 364–380 (2017).
- 825 43. Vohryzek, J., Deco, G., Cessac, B., Kringelbach, M. L. & Cabral, J. Ghost
826 Attractors in Spontaneous Brain Activity: Recurrent Excursions Into Functionally-
827 Relevant BOLD Phase-Locking States. en. *Front. Syst. Neurosci.* **14**, 20.
828 ISSN: 1662-5137 (Apr. 2020).
- 829 44. Rabuffo, G., Fousek, J., Bernard, C. & Jirsa, V. Neuronal Cascades Shape
830 Whole-Brain Functional Dynamics at Rest. en. *eNeuro* **8**. ISSN: 2373-2822
831 (Sept. 2021).
- 832 45. Cornblath, E. J. *et al.* Temporal sequences of brain activity at rest are con-
833 strained by white matter structure and modulated by cognitive demands.
834 en. *Commun Biol* **3**, 261. ISSN: 2399-3642 (May 2020).
- 835 46. Wong, K.-F. & Wang, X.-J. A recurrent network mechanism of time in-
836 tegration in perceptual decisions. *Journal of Neuroscience* **26**, 1314–1328
837 (2006).
- 838 47. Sanz-Leon, P. *et al.* The Virtual Brain: a simulator of primate brain net-
839 work dynamics. *Frontiers in neuroinformatics* **7** (2013).
- 840 48. Montbrió, E., Pazó, D. & Roxin, A. Macroscopic description for networks
841 of spiking neurons. *Physical Review X* **5**, 021028 (2015).
- 842 49. Van Essen, D. C. *et al.* The WU-Minn human connectome project: an
843 overview. *Neuroimage* **80**, 62–79 (2013).
- 844 50. Stephan, K. E., Weiskopf, N., Drysdale, P. M., Robinson, P. A. & Friston,
845 K. J. Comparing hemodynamic models with DCM. en. *Neuroimage* **38**,
846 387–401. ISSN: 1053-8119 (Nov. 2007).
- 847 51. Deco, G. & Jirsa, V. K. Ongoing cortical activity at rest: criticality, multi-
848 stability, and ghost attractors. en. *J. Neurosci.* **32**, 3366–3375. ISSN: 0270-
849 6474, 1529-2401 (Mar. 2012).

- 850 52. Haimovici, A., Tagliazucchi, E., Balenzuela, P. & Chialvo, D. R. Brain
851 organization into resting state networks emerges at criticality on a model
852 of the human connectome. en. *Phys. Rev. Lett.* **110**, 178101. ISSN: 0031-
853 9007, 1079-7114 (Apr. 2013).
- 854 53. Sporns, O., Faskowitz, J., Teixeira, A. S., Cutts, S. A. & Betzel, R. F. Dy-
855 namic expression of brain functional systems disclosed by fine-scale analysis
856 of edge time series. en. *Netw. Neurosci.* **5**, 405–433. ISSN: 2472-1751 (Apr.
857 2021).
- 858 54. Pope, M., Fukushima, M., Betzel, R. F. & Sporns, O. Modular origins of
859 high-amplitude cofluctuations in fine-scale functional connectivity dynam-
860 ics. en. *Proc. Natl. Acad. Sci. U. S. A.* **118**. ISSN: 0027-8424, 1091-6490
861 (Nov. 2021).
- 862 55. Cocchi, L., Gollo, L. L., Zalesky, A. & Breakspear, M. Criticality in the
863 brain: A synthesis of neurobiology, models and cognition. en. *Prog. Neu-
864 robiol.* **158**, 132–152. ISSN: 0301-0082, 1873-5118 (Nov. 2017).
- 865 56. Kong, X. *et al.* Sensory-motor cortices shape functional connectivity dy-
866 namics in the human brain. en. *Nat. Commun.* **12**, 6373. ISSN: 2041-1723
867 (Nov. 2021).
- 868 57. Fox, M. D. & Raichle, M. E. Spontaneous fluctuations in brain activity
869 observed with functional magnetic resonance imaging. en. *Nat. Rev. Neu-
870 rosci.* **8**, 700–711. ISSN: 1471-003X (Sept. 2007).
- 871 58. Mitra, A. *et al.* Spontaneous Infra-slow Brain Activity Has Unique Spa-
872 tiotemporal Dynamics and Laminar Structure. en. *Neuron* **98**, 297–305.e6.
873 ISSN: 0896-6273, 1097-4199 (Apr. 2018).
- 874 59. Margulies, D. S. *et al.* Situating the default-mode network along a principal
875 gradient of macroscale cortical organization. en. *Proc. Natl. Acad. Sci. U.
876 S. A.* **113**, 12574–12579. ISSN: 0027-8424, 1091-6490 (Nov. 2016).
- 877 60. Huntenburg, J. M., Bazin, P.-L. & Margulies, D. S. Large-Scale Gradients
878 in Human Cortical Organization. en. *Trends Cogn. Sci.* **22**, 21–31. ISSN:
879 1364-6613, 1879-307X (Jan. 2018).
- 880 61. Ashwin, P., Creaser, J. & Tsaneva-Atanasova, K. Fast and slow domino
881 regimes in transient network dynamics. en. *Phys Rev E* **96**, 052309. ISSN:
882 2470-0053, 2470-0045. arXiv: 1701.06148 [math.DS] (Nov. 2017).
- 883 62. Ashwin, P., Creaser, J. & Tsaneva-Atanasova, K. Sequential escapes: onset
884 of slow domino regime via a saddle connection. *Eur. Phys. J. Spec. Top.*
885 **227**, 1091–1100. ISSN: 1951-6355, 1951-6401 (Nov. 2018).
- 886 63. Deco, G., Senden, M. & Jirsa, V. How anatomy shapes dynamics: a semi-
887 analytical study of the brain at rest by a simple spin model. en. *Front.*
888 *Comput. Neurosci.* **6**, 68. ISSN: 1662-5188 (Sept. 2012).
- 889 64. Kim, J., Joshi, A., Frank, L. & Ganguly, K. Cortical–hippocampal cou-
890 pling during manifold exploration in motor cortex. *Nature*. ISSN: 14764687
891 (2022).

- 892 65. Chaudhuri, R., Gerçek, B., Pandey, B., Peyrache, A. & Fiete, I. The intrinsic attractor manifold and population dynamics of a canonical cognitive
893 circuit across waking and sleep. *Nature Neuroscience* **22**, 1512–1520. ISSN:
894 15461726 (2019).
895
- 896 66. Favaretto, C. *et al.* Subcortical-cortical dynamical states of the human
897 brain and their breakdown in stroke. *Nature Communications* **13**. ISSN:
898 20411723 (2022).
- 899 67. Rué-Queralt, J. *et al.* Decoding brain states on the intrinsic manifold of
900 human brain dynamics across wakefulness and sleep. *Communications Bi-*
901 *ology* **4**, 1–11. ISSN: 23993642 (2021).
- 902 68. Gao, S., Mishne, G. & Scheinost, D. Nonlinear manifold learning in func-
903 tional magnetic resonance imaging uncovers a low-dimensional space of
904 brain dynamics. en. *Hum. Brain Mapp.* **42**, 4510–4524. ISSN: 1065-9471,
905 1097-0193 (Oct. 2021).
- 906 69. Michel, C. M. & Koenig, T. EEG microstates as a tool for studying the
907 temporal dynamics of whole-brain neuronal networks: A review. en. *Neu-*
908 *roimage* **180**, 577–593. ISSN: 1053-8119, 1095-9572 (Oct. 2018).
- 909 70. Britz, J., Van De Ville, D. & Michel, C. M. BOLD correlates of EEG
910 topography reveal rapid resting-state network dynamics. *Neuroimage* **52**,
911 1162–1170 (2010).
- 912 71. Bréchet, L. *et al.* Capturing the spatiotemporal dynamics of self-generated,
913 task-initiated thoughts with EEG and fMRI. en. *Neuroimage* **194**, 82–92.
914 ISSN: 1053-8119, 1095-9572 (July 2019).
- 915 72. Drew, P. J., Mateo, C., Turner, K. L., Yu, X. & Kleinfeld, D. Ultra-slow
916 oscillations in fMRI and resting-state connectivity: neuronal and vascular
917 contributions and technical confounds. *Neuron* **107**, 782–804 (2020).
- 918 73. Wang, X.-J. Macroscopic gradients of synaptic excitation and inhibition in
919 the neocortex. *Nature Reviews Neuroscience* **21**, 169–178 (2020).
- 920 74. Chaudhuri, R., Knoblauch, K., Gariel, M. A., Kennedy, H. & Wang, X. J.
921 A Large-Scale Circuit Mechanism for Hierarchical Dynamical Processing
922 in the Primate Cortex. *Neuron* **88**, 419–431. ISSN: 10974199 (2015).
- 923 75. Wang, P. *et al.* Inversion of a large-scale circuit model reveals a cortical hi-
924 erarchy in the dynamic resting human brain. *Science advances* **5**, eaat7854
925 (2019).
- 926 76. Mesulam, M. M. From sensation to cognition. en. *Brain* **121** (Pt 6),
927 1013–1052. ISSN: 0006-8950 (June 1998).
- 928 77. Shine, J. M. *The thalamus integrates the macrosystems of the brain to*
929 *facilitate complex, adaptive brain network dynamics* 2020.
- 930 78. Kringelbach, M. L. *et al.* Dynamic coupling of whole-brain neuronal and
931 neurotransmitter systems. *Proceedings of the National Academy of Sciences*
932 **117**, 9566–9576 (2020).

- 933 79. Aquino, K. M. *et al.* On the intersection between data quality and dynamical modelling of large-scale fMRI signals. *NeuroImage* **256**, 119051. ISSN: 10959572 (2022).
- 934
- 935
- 936 80. Van De Ville, D., Farouj, Y., Preti, M. G., Liégeois, R. & Amico, E. When makes you unique: temporality of the human brain fingerprint. *Science advances* **7**, eabj0751 (2021).
- 937
- 938
- 939 81. Amunts, K., Mohlberg, H., Bludau, S. & Zilles, K. Julich-Brain: A 3D probabilistic atlas of the human brain's cytoarchitecture. *Science* **369**, 988–992. ISSN: 10959203 (2020).
- 940
- 941
- 942 82. Schirner, M. *et al.* Brain simulation as a cloud service: The Virtual Brain on EBRAINS. *NeuroImage* **251**, 118973. ISSN: 10959572 (2022).
- 943
- 944 83. Müller, E. J., Munn, B. R. & Shine, J. M. Diffuse neural coupling mediates complex network dynamics through the formation of quasi-critical brain states. *Nat. Commun.* **11**. ISSN: 2041-1723 (Dec. 2020).
- 945
- 946
- 947 84. Munn, B. R., Müller, E. J., Wainstein, G. & Shine, J. M. The ascending arousal system shapes neural dynamics to mediate awareness of cognitive states. en. *Nat. Commun.* **12**, 6016. ISSN: 2041-1723 (Oct. 2021).
- 948
- 949
- 950 85. Cisek, P. Resynthesizing behavior through phylogenetic refinement. en. *Atten. Percept. Psychophys.* **81**, 2265–2287. ISSN: 1943-3921, 1943-393X (Oct. 2019).
- 951
- 952
- 953 86. Domhof, J. W. M., Jung, K., Eickhoff, S. B. & Popovych, O. V. Parcellation-induced variation of empirical and simulated brain connectomes at group and subject levels. *Network Neuroscience* **5**, 798–830 (2021).
- 954
- 955
- 956 87. Sanz-Leon, P., Knock, S. A., Spiegler, A. & Jirsa, V. K. Mathematical framework for large-scale brain network modeling in The Virtual Brain. *NeuroImage* **111**, 385–430 (2015).
- 957
- 958
- 959 88. Trebaul, L. *et al.* Probabilistic functional tractography of the human cortex revisited. en. *Neuroimage* **181**, 414–429. ISSN: 1053-8119, 1095-9572 (Nov. 2018).
- 960
- 961
- 962 89. Desikan, R. S. *et al.* An automated labeling system for subdividing the human cerebral cortex on MRI scans into gyral based regions of interest. en. *Neuroimage* **31**, 968–980. ISSN: 1053-8119 (July 2006).
- 963
- 964
- 965 90. Allen, E. A. *et al.* Tracking whole-brain connectivity dynamics in the resting state. en. *Cerebral Cortex* **24**, 663–676. ISSN: 1047-3211, 1460-2199 (Mar. 2014).
- 966
- 967
- 968 91. Preti, M. G. & Van De Ville, D. Decoupling of brain function from structure reveals regional behavioral specialization in humans. en. *Nat. Commun.* **10**, 4747. ISSN: 2041-1723 (Oct. 2019).
- 969
- 970
- 971 92. Yamapi, R., Filatrella, G & Aziz-Alaoui, M. A. Global stability analysis of birhythmicity in a self-sustained oscillator. en. *Chaos* **20**, 013114. ISSN: 1054-1500, 1089-7682 (Mar. 2010).
- 972
- 973

- 974 93. Vos de Wael, R. *et al.* BrainSpace: a toolbox for the analysis of macroscale
975 gradients in neuroimaging and connectomics datasets. en. *Commun Biol*
976 **3**, 103. ISSN: 2399-3642 (Mar. 2020).
- 977 94. Domhof, J. W. M., Jung, K., Eickhoff, S. B. & Popovych, O. V. *Parcellation-*
978 *based resting-state blood-oxygen-level-dependent (BOLD) signals of a healthy*
979 *cohort (v1.0)* 2022.